Peer-reviewed version available at *Materials* **2019**, *12*, 2944; doi:10.3390/ma12182944

Effect of Welding Thermal Cycles on Microstructure and Mechanical Properties of Multi-Strand Composite Welding Wire Welded Joints of High Nitrogen Austenitic Stainless Steel

Jianguo Li[a, b], Huan Li[a, b], Yu Liang[c], Pingli Liu[c], LijunYang[a, b, *]

[a] School of Materials Science and Engineering, Tianjin University, Tianjin 300072, China;

[b] Tianjin Key Laboratory of Advanced Joining Technology, Tianjin 300072, China.

[c] Jiangsu Lianjie Welding Technology Co., Jiangsu 214400, China

[*] Corresponding author. Tel: +8613622152352

E-mail address: JGLi1991@163.com (Jianguo Li); lihuan@tju.edu.cn (Huan Li);

Liangyu@lianjiehanye.com (Yu Liang); liupl001@163.com (Liu Pingli);

yljabc@tju.edu.cn (Lijun Yang).

Abstract

A multi-strand composite welding wire was applied to join high nitrogen austenitic stainless steel, and microstructures and mechanical properties were investigated. The electrical signals demonstrate that the welding process using a multi-strand composite welding wire is highly stable. The welded joints are composed of columnar austenite and dendritic ferrite and welded joints obtained under high heat input and cooling rate have a noticeable coarse-grained heat-affected zone and larger columnar austenite in weld seam. Compared with welded joints obtained under the high heat input and cooling rate, welded joints have the higher fractions of deformed grains, high angle grain boundaries, Schmid factor and the lower dislocation density under the low heat input and cooling rate, which indicate a lower tensile strength and higher yield strength. The rotated goss (G_{RD}) ($\{110\}\langle 1\bar{1}0\rangle$) orientation of a thin plate and the cube (C) ($\{001\}\langle 100\rangle$) orientation of a thick plate are obvious after welding, but the S ($\{123\}\langle 63\bar{4}\rangle$) orientation at 65° sections of Euler's space is weak. The δ-ferrite was studied based on

Peer-reviewed version available at *Materials* **2019**, *12*, 2944; doi:10.3390/ma12182944

the primary ferrite solidification mode. It is observed that low heat input and high cooing rate result in the increasing of δ-ferrite and high dislocation density was obtained in grain boundaries of δ-ferrite. $M_{23}C_6$ precipitates due to low cooling rate and heat input in weld seam and deteriorates the elongation of welded joints. The engineering stress-strain curves also show the low elongation and tensile strength of welded joints under low heat input and cooling rate, which is mainly caused by the high fraction of δ-ferrite and the precipitation of $M_{23}C_6$.

Keywords: High nitrogen austenitic stainless steel; Multi-strand composite welding wire; EBSD; Welding thermal cycle; Mechanical property; Microstructure

1. Introduction

High nitrogen austenitic stainless steel (HNASS) is a novel engineering material utilising nitrogen (>0.4 %), which is used as a substitute for nickel in conventional high-nickel austenitic stainless steel. Nitrogen is a strengthening interstitial element which improves the mechanical strength and corrosion resistance of materials and enlarges the austenite range [1, 2]. Additionally, nitrogen reduces allergic reactions and the high cost of conventional austenitic stainless steel due to nickel. Therefore, HNASS is widely used in power plants, shipbuilding, petroleum, pressure vessels, and the medical industry. However, the application of HNASS in structural components is limited by many welding issues. Kamiya et al. [3] reported the loss of nitrogen and porosities observed in welding. Ogawa et al. [4] reported nitride precipitation behaviours at the welding heat-affected zone (HAZ) of high nitrogen stainless steel. The solidification cracking due to the reduction of δ-ferrite was studied by Woo and Kikuchi [5]. These phenomena greatly reduce the mechanical properties and corrosion resistance of welded joints.

To solve these issues, Hertzman [6] reported that the nitrogen loss of weld pools was avoided by

Peer-reviewed version available at *Materials* **2019**, *12*, 2944; doi:10.3390/ma12182944

controlling the shielding gas nitrogen content in tungsten inert gas (TIG) welding. Hosseini et al. [7] also demonstrated that nitrogen loss resulted in the formation of large ferrites and nitrides and recommended using shielding gases containing-nitrogen and filler metals. Qiang and Wang [8] employed the double-sided synchronous autogenous gas tungsten arc welding (GTAW) and studied effect of shielding gases on HNASS welding. However, this process is relatively unstable. Additionally, friction stir welding (FSW), which is a solid-state welding process, was first adopted by Park et al. [9]. Li et al. [10] obtained a higher yield strength and ultimate tensile strength than base metals in the welding process of HNASS using FSW, but the elongation was reduced significantly. Shielded metal arc welding, GTAW, electron beam welding, and FSW processes were compared by Mohammed et al. [11], and improved mechanical properties were obtained in FSW compared to fusion welds. However, good support for workpieces is required in FSW and this process is not practical for complicated shape components welding.

For applications, gas metal arc welding (GMAW) is the most convenient, reliable, and widely used welding technique. Cortes-Cervantes et al. [12] used GMAW to join super-austenitic stainless steel and studied the electromagnetic interactions. Toit [13] employed E307, ER2209, and 15CrMn to join Cromanite, and E307 produced sound weld joints with excellent mechanical properties. However, no matching filler metals can be used to join HNASS at present. A multi-strand composite welding wire is proposed as rotating wire to join HNASS in GMAW. Zhang et al. [14] also reported that the rotating wire GMAW process changes the fluid flow of molten pools, refined microstructure, and markedly improves the tensile strength. Moreover, for high nitrogen stainless steel, microstructure and mechanical properties of welded joint are sensitive to heat input and cooling rate during welding. Hence, the study on microstructure and mechanical properties of welded joints combined under the

Peer-reviewed version available at *Materials* **2019**, *12*, 2944; doi:10.3390/ma12182944

different welding thermal cycles by the multi-strand composite welding wire is very necessary. Electron backscatter diffraction (EBSD) is a promising technique which is widely used by material researchers, scientists, and engineers. Randle [15] demonstrated that this technique can measure microtexture and microstructure fractions, characterise the grain and phase boundaries, identify phases, and determine the strain.

Herein, HNASSs are joined under the different thermal cycles by multi-strand composite welding wire GMAW. The microstructures and local plastic strain of weld joints are estimated by measuring the dislocation density, misorientation angle, recrystallised grains, Schmid factor, and crystal orientation via EBSD. The mechanical properties were measured by a tensile test, and the fracture micrographs were observed. To further study the strengthening mechanism, microstructures of weld seam were investigated.

2. Experimental procedures

HNASS was joined by a multi-strand composite welding wire called TP-N1670. The welding wires TP-N1670 were provided by Jiangsu Lianjie Welding Technology Co., Ltd. HNASS plates with different dimensions of 300 mm × 150 mm × 14 mm (1670-14) and 300 mm × 150 mm × 8 mm (1670-8) were applied. The maximum diameter of the welding wire was 1.6 mm. The welding wire, as illustrated in Fig. 1, was composed of seven wires with a diameter of 0.53 mm, and the equivalent diameter was 1.4 mm. In Fig. 1, L represents the feeding length when welding wire rotated a cycle, and for TP-N1670, L measured 12.5 mm. The chemical compositions of the HNASS and the welding wire are listed in Table 1.

Peer-reviewed version available at Materials 2019, 12, 2944; doi:10.3390/ma12182944

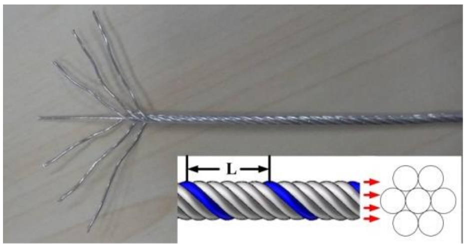

Fig. 1 Schematic of welding wire.

Welding trials for the different HNASSs were conducted. The equipment system for the welding trials is presented in Fig. 2. The main system components consisted of a power source, welding torch, electrical signal acquisition system, thermocouple, and temperature acquisition system. The EWM welding power source was operated in direct current electrode positive (DCEP) condition, and a shielding gas of 97.5 % Ar + 2.5 % CO_2 was used in the welding process. The welding parameters for HNASSs were kept consistent, as presented in Table 2. The current and voltage waveforms were obtained by using an electrical signal acquisition system with a sampling rate of 100 kHz. Moreover, a DEWETRON temperature acquisition system was used to obtain the welding thermal cycle curves. The type K thermocouples with a range from 0 to 1100 °C were glued to the bottom surface using aluminium tape, and the distance from the weld seam centre was 6 mm.

Table 1 Chemical compositions of the base metal, welding wires and weld seams.

Materials	C	Mn	Cr	Ni	Mo	N	Si	P	S	Fe
HNASS (wt. %)	0.05	18.75	21.12	2.24	0.13	0.68	0.38	0.02	0.01	Bal.
TP-N1670 (wt. %)	0.07	6.62	18.96	8.58	0.01	0	0.85	0.02	0.02	Bal.
1670-8 (wt. %)	0.06	8.78	19.54	7.67	0.08	0.14	0.83	0.02	0.02	Bal.
1670-14 (wt. %)	0.07	8.65	19.38	7.94	0.07	0.14	0.80	0.02	0.02	Bal.

After welding, the tensile test samples were cut perpendicularly to the welded joints. The tensile tests were conducted at a strain rate of 0.5 s^{-1}, and the fracture surfaces were observed using scanning electron microscopy (SEM). The transverse sections of the welded joints with different thicknesses are presented in Fig. 3. It is observed that the welded joints of 1670-8 and the 1670-14 are composed of three passes and four passes, respectively. The chemical compositions of weld seam were measured by X-ray fluorescence spectrograph (Axios), and nitrogen contents were measured by Oxygen and Nitrogen Analyzer (EMGA-820), as shown in Table 1. The microstructures of the welded joints were characterised with optical microscopy (OM) and the EBSD system equipped with an SEM. The locations observed were marked in Fig. 3, and the red boxes indicate the location of the EBSD study and green cycles indicate the OM study. The OM samples were machined from the welded joints, ground, mechanically polished, and etched in a mixed reagent of HCl and HNO_3 (3:1) for 30 s. The EBSD samples were prepared by grinding, mechanically polishing, and electrolytically polishing in a reagent of ethyl alcohol and perchloric acid (15:85, volume fraction) at 20 V for 15 s. For the identification of precipitates and investigation of deformation mechanism, transmission electron microscopy (TEM) was applied.

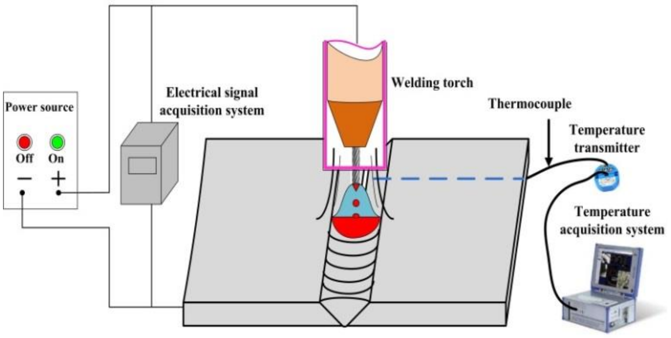

Fig. 2 Schematic diagram of the welding trials.

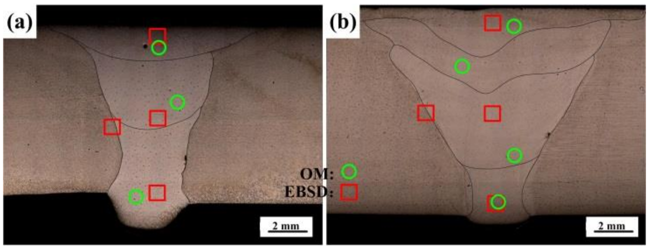

Fig. 3 Transverse section of the welded joints for the (a) 1670-8 and (b) 1670-14.

Peer-reviewed version available at *Materials* **2019**, *12*, 2944; doi:10.3390/ma12182944

Table 2 Welding parameters.

	Pass	Welding current (A)	Welding voltage (V)	Welding speed (mm/min)	Heat input (KJ/cm)
Thin plate	1	150	16.9	491	3.1
	2	250	25.5	411	9.3
	3	250	25.5	379	10.1
Thick plate	1	160	17.8	335	5.1
	2	250	25.2	356	10.6
	3	250	26.7	356	11.2
	4	250	26.7	356	11.2

3. Results and discussion

3.1 Welding thermal cycle and electrical signal

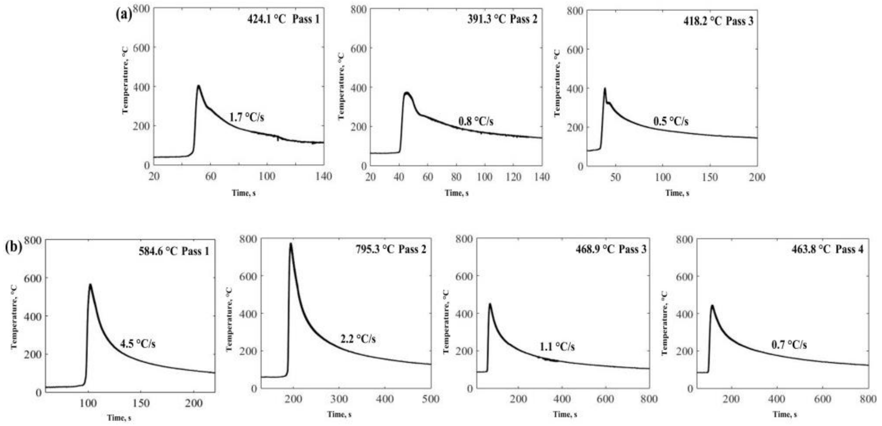

Fig. 4 Thermal cycle curves for each pass during welding for the (a) 1670-8 and (b) 1670-14.

The HNASS plates with different thicknesses were joined by GMAW using a multi-strand composite welding wire. The thermal cycle curves measured can clearly illustrate the change in heat input and cooling rate during welding. Table 2 displays a higher heat input for 1670-14. Fig. 4 presents the thermal cycle curves at 6 mm from the welding seam centre. According to Fig. 4(a), the peak temperature of 1670-14 at every pass is higher than that of 1670-8 in the welding process. Moreover, as observed in Fig. 4(b), 1670-14 has a higher average cooling rate than 1670-8 at the first pass, and the average cooling rate of 1670-14 decreases with the increase of the current and voltage. Fig. 5 shows the current waveforms, voltage waveforms. The current and voltage waveforms at pass 1 reflect a highly stable short-circuiting transfer process, and a high short-circuiting transfer frequency reveals the stability and homogeneity of the droplet transfer. The low mean square deviation also reflects a stable welding droplet transfer process. During the welding, when the arc shortens, the voltage value decreases. The voltage and current waveforms of 1670-8 and 1670-14 at other passes have little fluctuation, which indicates that the modes of the droplet transfer represent the spray transfer, and the stability is higher than that of short-circuiting transfers. Moreover, it is observed that the welding process of 1670-14 is more stable than that of 1670-8.

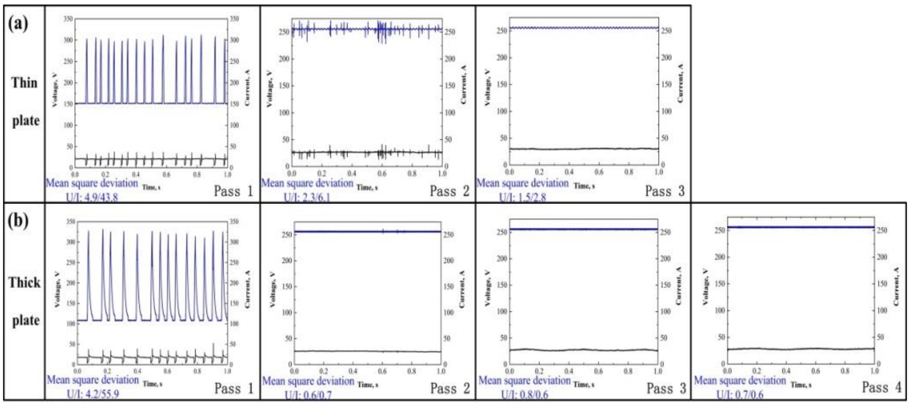

Fig. 5 Electrical signal oscillograms for the (a) 1670-8 and (b) 1670-14. U/I represents the square deviation value of the thin and thick plates in 1 s.

3.2 Microstructures of the welded joints

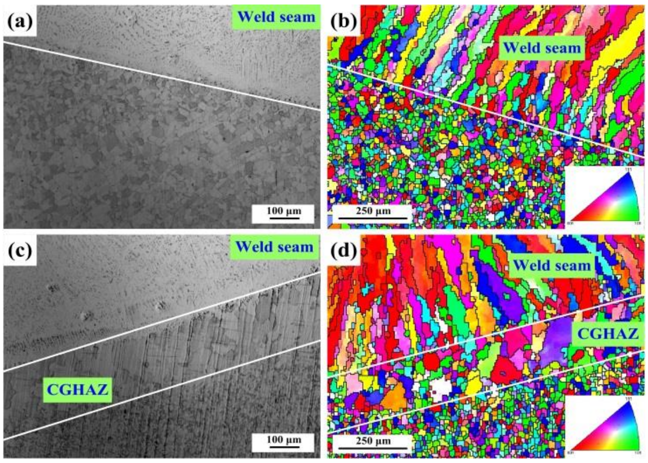

Fig. 6 Microstructures (a) observed by OM and (b) inverse pole figure (IPF) for 1670-8, and (c) observed by OM and (d) IPF for 1670-14.

The OM and EBSD maps of the welded joints are observed in Fig. 6. The base metal is composed of equiaxed austenite, and the weld seam is composed of columnar austenite and dendritic δ-ferrite. Following the welding thermal cycles, the weld seam produces a preferential growth of columnar grains. The grains of the base metal in the vicinity of the fusion line are affected, and the recovery and recrystallisation occur. High heat input is in favour of the growth of columnar grains and the formation of coarse-grained heat-affected zone (CGHAZ). Therefore, 1670-14 has larger columnar grains, and the CGHAZ is produced due to the local high heat input of the base metal. The maximum width of the CGHAZ is 240 μm. As 1670-8 has low heat input, the CGHAZ is not formed.

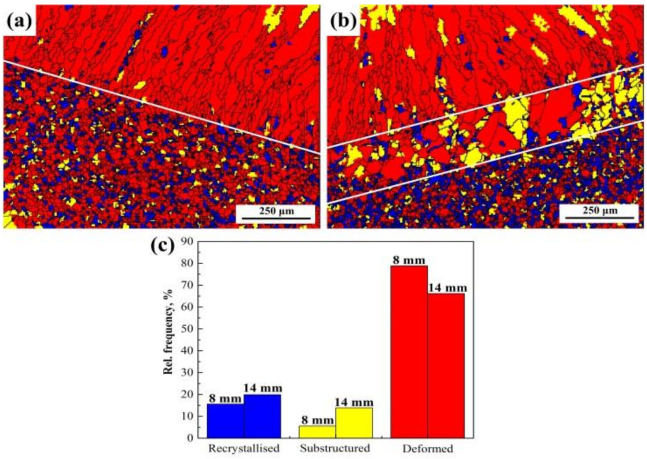

Fig. 7 Recrystallised grain distribution diagram for (a) 1670-8 and (b) 1670-14, and (c) the fraction of grains for the different thickness welded joints.

The grains of the welded joints change after the welding. When the average angle of a grain is greater than 3°, the grain is called a deformed grain. When the average angle is smaller than 3°, and the misorientation angle between grains is greater than 3°, the grain is called subgrains. The interface between adjoining grains is called sub-boundaries. The remaining grains are called recrystallised grains. From Fig. 7(a) and (b), it can be observed that the deformed grains gather in the weld seam, and the weld seam has few subgrains and recrystallised grains. The subgrain fraction of 1670-14 is higher than that of 1670-8 in the weld seam. Moreover, the recrystallised grains form along the deformed grains, which mainly results from the high driving force of nucleation in the deformed grains. The CGHAZ of 1670-14 is mainly composed of subgrains and deformed grains. According to Fig. 7(c), the percentage of recrystallised grains, subgrains, and deformed grains for 1670-14 is 20 %, 14 % and 66 %, respectively, while 1670-8 due to the lower heat input and the less number of pass presents a higher percentage of deformed grains (79 %) and a lower percentage of subgrains (5 %). In fact, the fraction of sub-boundaries rises with the increase of subgrains. Lu et al. [16] reported that the high sub-boundary fraction reflects the high dislocation density.

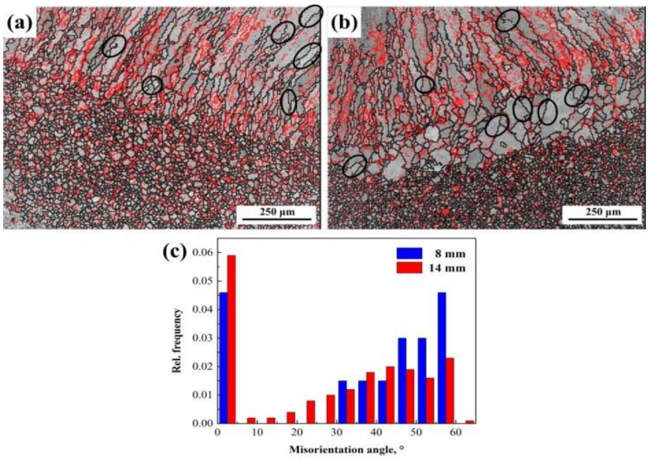

Fig. 8 Grain boundary maps for the (a) 1670-8, (b) 1670-14, and (c) the relative frequency of misorientation angle.

Figs. 8(a) and (b) represent the grain boundary distributions, and red line describe the low angle grain boundaries (LAGBs) (2°–15°), and the black line describe the high angle grain boundaries (HAGBs) (>15°). Fig. 8(c) shows the relative frequency of misorientation angle. The welded joint of 1670-14 presents a higher percentage of LAGBs in the selective area (32.4 %) than that of 1670-8. The regions with a high percent of LAGBs indicate a high degree of sensitization to concentration of dislocation density. Parts of HAGBs are marked in black cycle. From Fig. 7 and Fig. 8, it can be deduced that most of the recrystallised grains are formed along the HAGBs. Mccabe et al. [17] also reported that recrystallisation occurs because of the motion of HAGBs and the nucleation is preferentially formed close to HAGBs. High heat input and number of welding passes improve the formation of recrystallized grains along HAGB.

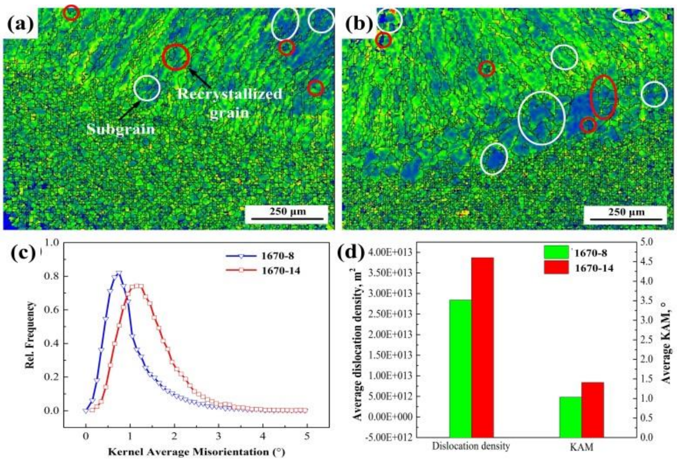

Fig. 9(a) KAM map of 1670-8, (b) KAM map of 1670-14, (c) KAM distribution, and (d) average dislocation density.

Owing to the preferential growth of grains in the weld seam and grain coarsening in the HAZ, parts of the neighbouring grains deform plastically during the welding, leading to the inhomogeneous local misorientation. Kamaya [18] reported that the local misorientation was consistent with the geometrically necessary dislocation density. The Kernel average misorientation (KAM) represents the average misorientation between neighbouring points. KAM maps reflect the distribution of the dislocation density. The measurement conditions and step size have a considerable influence on KAM maps, and all the measurements were conducted under the same conditions with a step size of 5 μm. The KAM maps of 1670-8 and 1670-14 are presented in Fig. 9(a) and Fig. 9(b), respectively. The dislocation density of 1670-14 is higher than that of 1670-8 in the weld seam. A sparse dislocation region is formed in the CGHAZ of 1670-14. As stated above, dislocations are mainly concentrated in deformed grains and sub-boundaries, and the dislocation density is low in subgrains and recrystallised grains, as observed in Fig. 9(a) and (b). The recrystallisation occurs easily in high dislocation density regions. The dislocation density decreases when the recrystallisation nucleation begins along deformed grains. Recrystallised grains form from deformed grains, which leads to the decrease of the dislocation density around recrystallised grains. Additionally, the HAGBs reduce the dislocation density, as observed in Fig. 8 and Fig. 9. Xu et al. [19] reported that the dislocation density was calculated as follows:

$$\rho = \frac{2\theta}{\mu b} \qquad [1]$$

Where ρ is the dislocation density of a point, θ is the local misorientation angle, μ is the unit length of the point, and b is the Burgers vector. Fig. 9(c) displays the KAM distribution in the selective area, and 1670-14 presents a larger KAM value than 1670-8. The average dislocation and KAM are calculated. Fig. 9(d) presents the average dislocation density and KAM. A high dislocation density leads to a large stress concentration with the increase of external force, and the plastic deformation has to overcome the considerable resistance of the dislocation accumulation. Moreover, weld seam is the weakest zone for HNASS, and determines the mechanical properties of welded joint. Therefore, high fractions of LAGB and dislocation density result in the stress concentration of 1670-14, which indicates that its welded joint has a better tensile strength than that of 1670-8 during deformation.

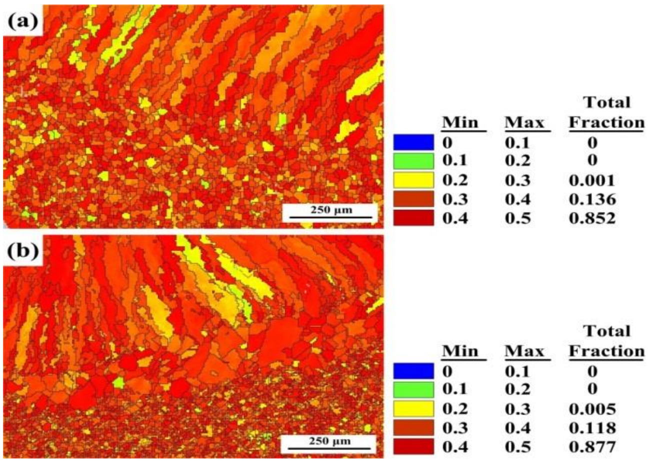

Fig. 10 Schmid factor of the different thicknesses of plates along the fusion line: (a) 1670-8 and (b) 1670-14.

The Schmid factors of welded joints calculated through the EBSD process are presented in Fig.

10. Gussevet al. [20] reported that the Schmid factor of soft grains is greater than 0.4, and that of hard grains is smaller than 0.35. Grains having a high Schmid factor are easier to slip. It can be observed that the welded joint of 1670-14 has a higher Schmid factor, and the grains oriented close to $\langle 101\rangle$ have the lowest Schmid factor, as shown in Fig. 6 and Fig. 10. The plastic deformation is easier for welded joint of 1670-14. In other words, welded joint of 1670-14 has the lower yield strength than that of 1670-8.

Fig. 11 presents the orientation distribution functions (ODFs) of the weld joints and the standard ODF for FCC materials at $\phi2 = 0°$, 45°, and 65° sections of Euler’s space. In contrast with a standard ODF, the ODF of 1670-8 at $\phi2 = 0°$, 45° clearly shows a typical rotated Goss (G_{RD}) ($\{110\}\langle 1\bar{1}0\rangle$) orientation, whereas the ODF of 1670-14 at the same Euler’s space presents the cube (C) ($\{001\}\langle 100\rangle$) orientation. All changes in grain orientation are probably due to the different thermal cycle. The thermal cycle also weakens the intensity of the S ($\{123\}\langle 63\bar{4}\rangle$) orientation at 65° sections of Euler's space.

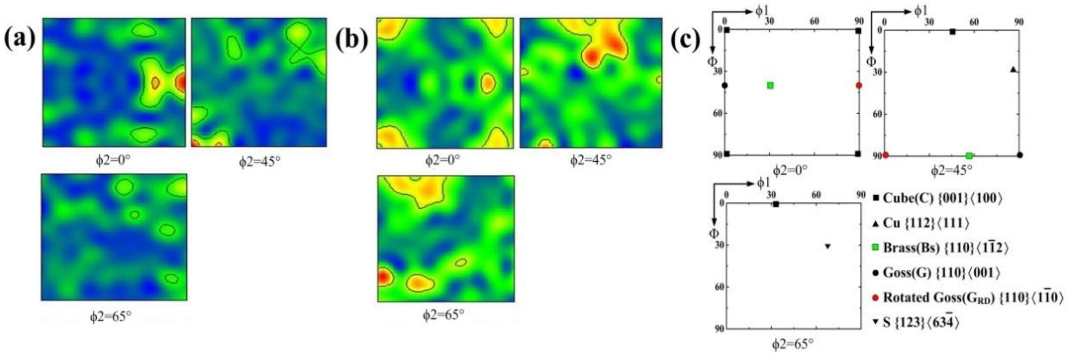

Fig. 11 Orientation distribution function sections of Euler's space for the (a) 1670-8, (b) 1670-14, and (c) standard ODF for FCC material.

3.3 Microstructures of the weld seam

After welding using the multi-strand composite welding wire, the microstructures in the weld seam are different from that of the base metal, which depends on the solidification modes. Hammar and

Svensson [21] established a relationship between the composition and solidification mode using Cr_{eq}/Ni_{eq}: $Ni_{eq}=Ni + 0.31Mn + 22C + 14.2N + Cu$ (wt. %) and $Cr_{eq} = Cr + 1.37Mo + 3Ti + 1.5Si + 2Nb$ (wt. %). The values of Cr_{eq}/Ni_{eq} for 1670-8 and 1670-14 are 1.53 and 1.61, respectively. Vasudevan et al. [22] reported that the primary ferrite mode C_{req}/Ni_{eq} ratio is greater than 1.5. Primary ferrite has a considerable influence on the properties of welded joints. Takalo et al. [23] reported that low ferrite welded joints with $Cr_{eq}/Ni_{eq} < 1.48$ were susceptible to hot-cracking. Lo et al. [24] reported that an austenite matrix containing ferrite presents favourable properties. Fig. 12 displays the OM of the weld seam at every pass. Figs. 12(a)-(c) represent the OM study of 1670-8 from bottom to top, and Figs. 12(d)-(g) represent that of 1670-14. It can be observed that the growth direction of dendritic δ-ferrite is affected by the temperature gradient direction of solidification. Jahanzed et al. [25] reported that the directionality of δ-ferrite reveals the low-temperature gradient and cooling rate in this region. The cooling rate reduces with the increasing of weld pass.

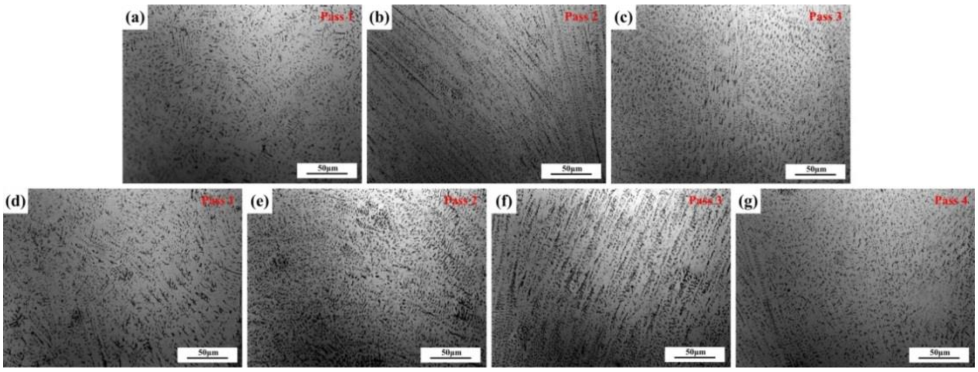

Fig. 12 Weld seam microstructures of plates of different thicknesses at each pass, (a), (b), and (c) for 1670-8 and (d), (e), (f), and (g) for 1670-14.

The effect of welding thermal cycle on microstructure was further studied, and amplified microstructures of weld seam from top to bottom were obtained in Fig. 13. According to the above mentioned, solidification of weld seam occurs in primary ferrite mode. When the cooling rate is high, the transformation of primary δ-ferrite into austenite is inhibited. Furthermore, thermal cycles of other passes can improve the transformation of δ-ferrite in pass 1, and have no effect on the top. For the top of welded joints, 1670-8 has the low heat input and cooling rate. However, the top of 1670-8 has a higher fraction of δ-ferrite, which indicates that the fraction of δ-ferrite increases with the decreasing of heat input. For the bottom of welded joints, the highest cooling rate and the lowest heat input should produce the highest fraction of δ-ferrite, but thermal cycles in other passes improve the change from network δ-ferrite to rod and granular δ-ferrite, as shown in Fig, 13.

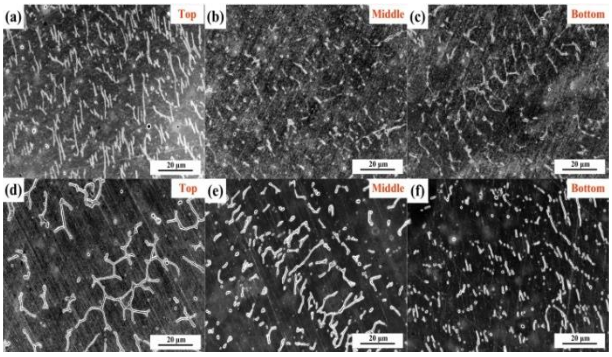

Fig. 13 SEM images of weld seam at the different places, (a), (b), and (c) for 1670-8 and (d), (e), and (f) for 1670-14.

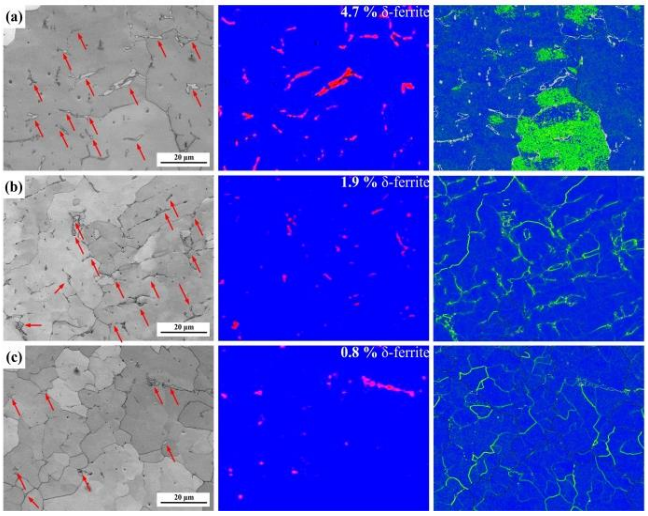

Fig. 14 Contrast maps, phase distribution maps, and KAM of 1670-8 at different places: (a) top, (b) middle, and (c) bottom.

In order to investigate the local misorientation of δ-ferrite, the weld seam was observed through

EBSD in a fine step size of 0.2 μm and a scanning area of 80 × 80 μm^2. Fig. 14 shows the contrast maps, phase maps, and KAM maps of 1670-8 in the weld seam. The microstructures are composed of δ-ferrite and columnar austenite. The δ-ferrite is marked with red arrows in the contrast maps, and the corresponding phase distribution maps show the fractions and distributions of the δ-ferrite (red) and austenite (blue). The KAM maps reveal the relatively higher dislocation density along the δ-ferrite boundaries compared to the austenite boundaries. Thermal cycles of other passes result in the occurrence of recrystallisation and transformation of δ-ferrite, so the dislocation density also increases from bottom to top. Fig. 15 shows the contrast maps, phase maps, and KAM maps of 1670-14 in the weld seam. Similarly, the dislocation density increases from bottom to top, and the boundary of the δ-ferrite has a higher dislocation density than that in grains. The middle and bottom dislocations mainly occur in the boundaries, but the top austenite grains also have a high dislocation density. Compared to the weld seam of 1670-14, the weld seam of 1670-8 contains larger fraction of δ-ferrite due to the low heat input. Nage et al. [26] have found that the mechanical properties increase with the decreasing of δ-ferrite in weld seam.

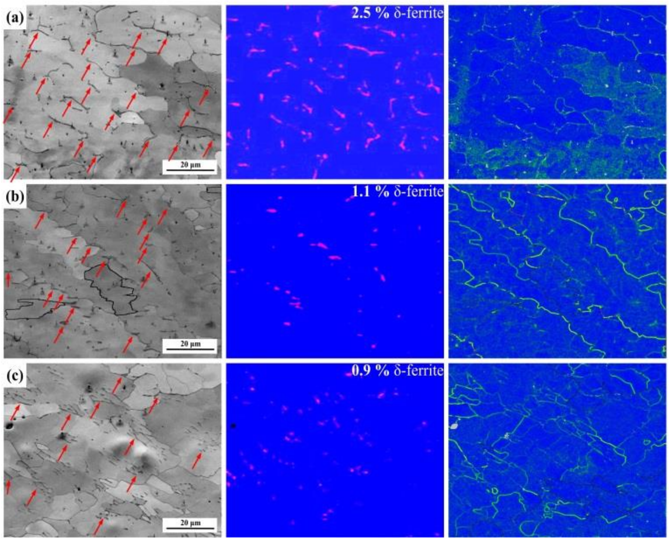

Fig. 15 Contrast maps, phase maps, and KAM maps of 1670-14 at different places: (a) top, (b) middle, and (c) bottom.

3.4 Mechanical properties after welding

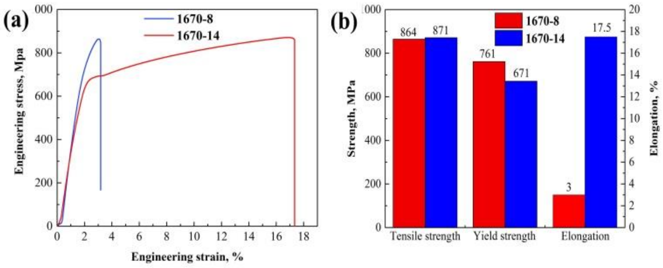

Fig. 16(a) stress-strain curve, (b) mechanical properties of the different welded joints.

To evaluate the strength and ductility of the welded joints, tensile tests were conducted at 25 °C. A fracture occurred in the weld seam. The tensile stress-strain curves are presented in Fig. 16(a), and it is observed in Fig. 16(b) that the welded joint of 1670-14 has higher elongation and tensile strength. As shown in Fig. 9, the welded seam of 1670-14 presents a higher dislocation density. It occurs easily for dislocation accumulation and stress concentration. Moreover, the high HAGBs of 1670-8 also represent the preferential crack nucleation sites. On the other hand, Lai et al. [27] reported that cracks initiate preferentially along the austenite/δ-ferrite interface, and high δ-ferrite leads to the elongation loss. After tensile tests, microstructures of welded joints were observed by TEM. Figs. 17(c) and (d) show that twins are found in weld seam and 1670-14 has a higher fraction of twins than 1670-8. Twin boundary, as a low energy boundary, has higher strength than random HAGB. Hence, 1670-14 has a higher tensile strength than 1670-8. We also found that $M_{23}C_6$ precipitates along grain boundary of austenite/δ-ferrite in weld seam of 1670-8, and grows into austenite matrix, as shown in Fig. 17(a). Zheng et al. [28] reported that the ductility of material reduce with the precipitation of $M_{23}C_6$. $M_{23}C_6$ is responsible for the low elongation of 1670-8.

Fig. 18 presents the fracture surface of the tensile samples, (a) and (c) represent the low magnitude fracture morphologies, and (b) and (d) represent the corresponding amplified morphologies of the red boxes. The typical ductility fracture features with dimples are shown in the fracture surfaces of 1670-8 and 1670-14, but fracture micrograph of 1670-14 presents relatively flat and homogeneous dimples. Deep and large holes marked in the cycle are formed in fracture surface of 1670-8. Moreover, 1670-14 presents transgranular dimples due to high stress concentration.

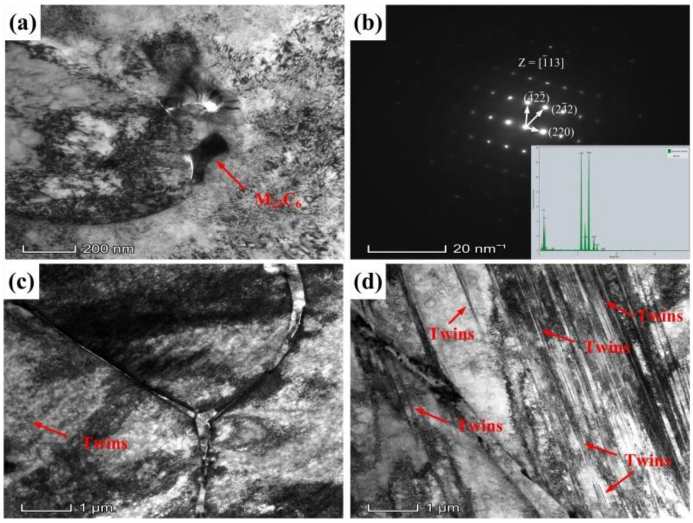

Fig. 17 TEM micrographs of the tensile samples of the welded joints: (a), (b) and (c) 1670-8, (d) 1670-14.

During the welding, the thermal cycle of the HAZ can reflect the heat input of the weld seam at every pass, as displayed in Fig. 4. The cooling rate reduces with the increase of the number of passes, and 1670-14 presents a higher cooling rate. After the welding, the metals of the weld seam solidify in the primary ferrite mode, then the primary ferrite transforms into austenite. The cooling rate considerably affects the transformation process, and the high cooling rate leads to large primary ferrite. High heat input increases the fraction of recrystallization grains, LAGBs and the local dislocation density of weld seam, which results in the high tensile strength. However, $M_{23}C_6$ precipitates in the weld seam of 1670-8 due to the low cooling rate, and reduces the elongation of welded joints.

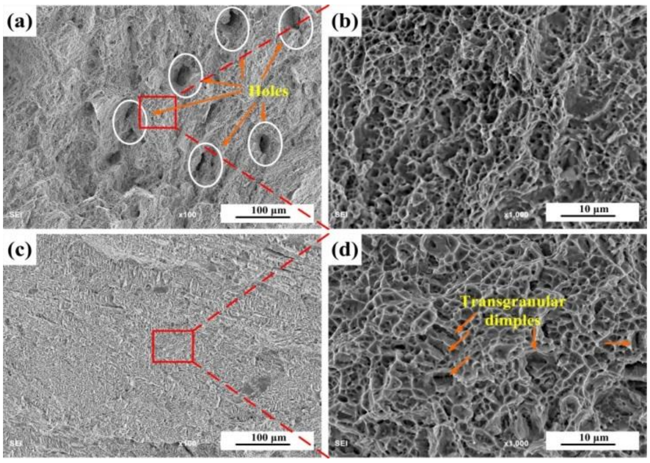

Fig. 18 Fracture micrographs of the tensile samples of the welded joints: (a) and (b) 1670-8, (c) and (d) 1670-14.

4. Conclusions

(1) The highly stable welding process and excellent welded joints of the HNASS using a multi-strand composite welding wire are obtained.

(2) After the welding, high heat input and cooling rate results in a noticeable CGHAZ and larger columnar austenite grains. The welded joint obtained under high heat input and cooling rate presents higher fractions of recrystallised grains, LAGBs, KAM, and dislocation density and lower Schmid factor, which indicates the higher tensile strength and the lower yield strength.

(3) The welded joint of the thin plate presents a strong intensity of rotated Goss (G_{RD}) ($\{110\}\langle 1\bar{1}0\rangle$) orientation, and the cube (C) ($\{001\}\langle 100\rangle$) orientation is observed in the welded joint of the thick plate. The S ($\{123\}\langle 63\bar{4}\rangle$) orientation at 65° sections of Euler's space is weak due to the thermal cycles.

(4) Low input and high cooling rate results in the increasing of primary ferrite in weld seam. The KAM maps reveal a high dislocation density around the primary ferrite. Low cooling rate leads to the precipitation of $M_{23}C_6$ in weld seam of 1670-8 and $M_{23}C_6$ deteriorates the elongation of welded joints.

doi:10.20944/preprints201908.0220.v1

Peer-reviewed version available at *Materials* **2019**, *12*, 2944; doi:10.3390/ma12182944

(5) Welded joint obtained under high heat input and cooling rate has low fraction of δ-ferrite, high tensile strength and elongation, which low heat input and cooling rate lead to the decreasing of elongation and tensile strength.

Acknowledgements

This work was supported by the National Natural Science Foundations of China (Gran No. 51675375).

Author Contributions: Conceptualization, J.L. and H.L.; Methodology, J.L. and H.L.; Software, J.L. and P.L.; Investigation, J.L. and L.Y.; Writing-original draft, J.L.; Writing-Review & Editing, J.L. and H.L.; Supervision, Y.L. and P.L.; Project Administration, Y.L. and L.Y.; Funding Acquisition, H.L; Resources, Y.L.; Formal analysis, J.L. and L.Y.; Data curation, J.L. and H.L.; Visualization, J.L. and L.Y.; Validation, H.L. and L.Y.

The authors declare no conflict of interest.

References

1 Katada, Y.; Washizu, N.; Baba, H. Development of high-nitrogen steels in the national institute for materials science. *Met. Sci. Heat Treat.* **2005**, 47, 494-496.

2 Byrnes, M.L.G.; Grujicic, M.; Owen, W.S. Nitrogen strengthening of a stable austenitic stainless steel. *Acta Metall.* **1987**, 35, 1853-1862.

3 Kamiya, O.; Chen, Z.W.; Kikuchi, Y. Microporosity formation in partially melted zone during welding of high nitrogen austenitic stainless steels. *J. Mater. Sci.* **2002**, 37, 2475-2481.

4 Ogawa, M.; Hiraoka, K.; Katada, Y.; Sagara, M.; Tsukamoto, S. Chromium nitride precipitation behavior in weld heat-affected zone of high nitrogen stainless steel. *ISIJ Int.* **2002**, 42, 1391-1398.

5 Woo, I.; Kikuchi, Y. Weldability of high nitrogen stainless steel. *ISIJ Int.* **2002**, 42, 1334-1343.

Peer-reviewed version available at *Materials* **2019**, *12*, 2944; doi:10.3390/ma12182944

6 Hertzman, S. The influence of nitrogen on microstructure and properties of highly alloyed stainless steel welds. *ISIJ Int.* **2001**, 41, 580-689.

7 Hosseini, V.A.; Wessman, S.; Hurtig, K.; Karlsson, L. Nitrogen loss and effects on microstructure in multipass TIG welding of a super duplex stainless steel. *Mater. Des.* **2016**, 98, 88-97.

8 Qiang, W.; Wang, K. Shielding gas effects on double-sided synchronous autogenous GTA weldability of high nitrogen austenitic stainless steel. *J. Mater. Process. Tech.* **2017**, 250, 169-181.

9 Park, S.H.C.; Sato, Y.S.; Kokawa, H. Microstructure of friction-stir-welded high-nitrogen stainless steel. *Mater. Sci. Forum.* **2007**, 539-543, 3757-3762.

10 Li, H.B.; Jiang, Z.H.; Feng, H.; Zhang, S.C.; Li, L.; Han, P.D.; Misra, R.D.K.; Li, J.Z. Microstructure, mechanical and corrosion properties of friction stir welded high nitrogen nickel-free austenitic stainless steel. *Mater. Des.* **2015**, 84, 291-299.

11 Mohammed, R.; Reddy, G.M.; Rao, K.S. Welding of nickel free high nitrogen stainless steel: Microstructure and mechanical properties. *Defence Technol.* **2017**, 13, 59-71.

12 Cortes-Cervantes, I.S.; Lopez-Morelos, V.H.; Miyashita, Y.; Garcia-Hernandez, R.; Ruiz-Marines, A. Garcia-Renteria, M.A. Fatigue resistance of AL6XN super-austenitic stainless steel welded with electromagnetic interaction of low intensity during GMAW. *Int. J. Adv. Manuf. Technol.* **2018**, 99, 2849-2862.

13 Tolt, M.D. Filler metal selection for welding a high nitrogen stainless steel. *J. Mater. Eng. Perform.* **2002**, 11, 306-312.

14 Zhang, H.T.; Chang, Q.; Liu, J.H.; Lu, H.; Wu, H.; Feng, J.C. A novel rotating wire GMAW process to change fusion zone shape and microstructure of mild steel. *Mater. Lett.* **2014**, 123, 101-103.

15 Randle, V. Electron backscatter diffraction: strategies for reliable data acquisition and processing.

Peer-reviewed version available at *Materials* **2019**, *12*, 2944; doi:10.3390/ma12182944

Mater. Charact. **2009**, 60, 913-922.

16 Lu, J.; Wu, X.; Liu, Z.; Chen, X.; Xu, B.; Wu, Z.; Ruan, S. Microstructure and mechanical properties of ultrafine-grained copper produced using intermittent ultrasonic-assisted equal-channel angular pressing. *Metall. Mater. Trans. A.* **2016**, 47, 4648-4658.

17 Mccabe, R.J.; Richards, A.W.; Clarke, K.D.; Beyerlein, I.J.; Knezevic, M. Microstructure effects on the recrystallization of low-symmetry alpha-uranium. *J. Nucl. Mater.* **2015**, 465, 189-195.

18 Kamaya, M.; Fonseca, J.Q.D.; Li, L.M.; Preuss, M. Local plastic strain measurement by EBSD. *Appl. Mech. Mater.* **2007**, 7-8, 173-179.

19 Xu, Y.; Nie, Y.; Wang, M.; Li, W.; Jin, X. The effect of microstructure evolution on the mechanical properties of martensite ferrite steel during long-term aging. *Acta Mater.* **2017**, 131, 110-122.

20 Gussev, M.N.; Field, K.G.; Busby, J.T. Deformation localization and dislocation channel dynamics in neutron-irradiated austenitic stainless steels. *J. Nucl. Mater.* **2015**, 460, 139-152.

21 Hammar, O.; Svensson, U. Influence of steel composition on segregation and microstructure during solidification of austenitic stainless steels. Solidification and Casting of Metals; The Metals Society: London, England, 1979, pp. 401-410.

22 Vasudevan, M.; Bhaduri, A.K.; Raj, B.; Rao, K.P. Artificial neural network modeling of solidification mode in austenitic stainless steel welds. *Mater. Sci. Technol.* **2007**, 23, 451-459.

23 Takalo, T.; Suutala, N.; Moisio, T. Austenitic solidification mode in austenitic stainless steel welds. *Metall. Trans. A.* **1979**, 10A, 1173-1181.

24 Lo, K.H.; Shek, C.H.; Lai, J.K.L. Recent developments in stainless steels. *Mater. Sci. Eng. R.* **2009**, 65, 39-104.

25 Jahanzeb, N.; Shin, J.H.; Singh, J.; Heo, Y.U.; Choi, S.H. Effect of microstructure on the hardness

Peer-reviewed version available at *Materials* **2019**, *12*, 2944; doi:10.3390/ma12182944

heterogeneity of dissimilar metal joints between 316L stainless steel and SS400 steel. *Mater. Sci. Eng. A.* **2017**, 700, 338-350.

26 Nage, D.D.; Raja, V.S.; Raman, R. Effect of nitrogen addition on the microstructure and mechanical behavior of 317L and 904L austenitic stainless steel welds. *J. Mater. Sci.* **2006**, 41, 2097-2112.

27 Lai, C.L.; Lu, W.F.; Huang, J.Y. Effect of δ-ferrite content on the stress corrosion cracking behavior of cast austenitic stainless steel in high-temperature water environment. *Corros.* **2014**, 70, 591-597.

28 Zheng, L.G.; Hu, X.Q.; Kang, X.H.; Li, D.Z. Precipitation of $M_{23}C_6$ and its effect on tensile properties of 0.3C-20Cr-11Mn-1Mo-0.35N steel. *Mater. Des.* **2015**, 78, 42-50.

Peer-reviewed version available at Materials 2019, 12, 2944; doi:10.3390/ma12182944

Figure and Table captions

Fig. 1 Schematic of a welding wire.

Fig. 2 Schematic diagram of the welding trials.

Fig. 3 Transverse section of the welded joints for the (a) 1670-8 and (b) 1670-14.

Fig. 4 Thermal cycle curves for each pass during welding for the (a) 1670-8 and (b) 1670-14.

Fig. 5 Electrical signal oscillograms for the (a) 1670-8 and (b) 1670-14. U/I represents the square deviation value of the thin and thick plates in 1 s.

Fig. 6 Microstructures (a) observed by OM and (b) inverse pole figure (IPF) for 1670-8, and (c) observed by OM and (d) IPF for 1670-14.

Fig. 7 Recrystallised grain distribution diagram for (a) 1670-8 and (b) 1670-14, and (c) the fraction of grains for the different thickness welded joints.

Fig. 8 Grain boundary maps for the (a) 1670-8, (b) 1670-14, and (c) relative frequency of misorientation angle.

Fig. 9(a) KAM map of 1670-8, (b) KAM map of 1670-14, (c) KAM distribution, and (d) average dislocation density.

Fig. 10 Schmid factor of the different thicknesses of plates along the fusion line: (a) 1670-8 and (b) 1670-14.

Fig. 11 Orientation distribution function sections of Euler's space for the (a) 1670-8, (b) 1670-14, and (c) standard ODF for FCC material.

Fig. 12 The weld seam microstructures of plates of different thicknesses at each pass,(a), (b), and (c) for 1670-8, and (d), (e), (f), and (g) for 1670-14.

Peer-reviewed version available at *Materials* **2019**, *12*, 2944; doi:10.3390/ma12182944

Fig. 13 SEM images of weld seam at the different places, (a), (b), and (c) for 1670-8 and (d), (e), and (f) for 1670-14.

Fig. 14 Contrast maps, phase distribution maps, and KAM of 1670-8 at different places: (a) top, (b) middle, and (c) bottom.

Fig. 15 Contrast maps, phase maps, and KAM maps of 1670-14 at different places: (a) top, (b) middle, and (c) bottom.

Fig. 16 (a) stress-strain curve, (b) mechanical properties of the different welded joints.

Fig. 17 TEM micrographs of the tensile samples of the welded joints: (a), (b) and (c) 1670-8, (d) 1670-14.

Fig. 18 Fracture micrographs of the tensile samples of the welded joints: (a) and (b) 1670-8, (c) and (d) 1670-14.

Table 1 Chemical compositions of the base metal, welding wires and weld seams.

Table 2 Welding parameters.